AALBORG UNIVERSITY

DENMARK

Damage resistant and tolerant glass-ceramics with low-thermal expansion crystals

Sun, Daming; Zhang, Qi; Du, Tao; Youngman, Randall E.; Jensen, Lars Rosgaard; Wang, Deyong; Yang, Feng; Klemmt, Rebekka; Smedskjær, Morten Mattrup

Link to publication from Aalborg University

Damage resistant and tolerant glass-ceramics with low-thermal expansion crystals

Daming Sun [a] , Qi Zhang [a], Tao Du [a], Randall E. Youngman [b], Lars R. Jensen [c] , Deyong Wang [c], Feng Yang [d], Rebekka Klemmt [e] , Morten M. Smedskjaer [a,*]

[a] *Department of Chemistry and Bioscience, Aalborg University, Aalborg, Denmark*
[b] *Science and Technology Division, Corning Incorporated, Corning, NY, USA*
[c] *Department of Materials and Production, Aalborg University, Aalborg, Denmark*
[d] *CDGM Glass Co., Ltd. Chengdu, China*
[e] *Interdisciplinary Nanoscience Center (iNANO) & iMAT Aarhus University Centre for Integrated Materials Research, Aarhus University, Aarhus, Denmark*

ARTICLE INFO

ABSTRACT

Crack initiation and growth limit the mechanical reliability and industrial applications of oxide glasses. The conversion of glasses into glass-ceramics can help to compensate for this shortcoming, as the presence of crystals can cause crack deflection and crack bridging and then increase the fracture toughness. However, due to the different thermal expansion of crystal and glass phases, the generation of residual stress is inevitable, which will induce compressive or tensile stress in glass-ceramics, thus changing the crack propagation path and crack initiation resistance. As such, it is a challenge to simultaneously improve the fracture toughness and crack initiation resistance. In this work, we attempt to address this challenge by modifying the crystal content in Nb_2O_5-doped magnesium aluminoborate glass-ceramics to improve crack resistance. Due to the generation of $Al_4B_2O_9$ crystals with a lower coefficient of thermal expansion compared to the glass matrix, compressive stress is generated on the surface of the glass-ceramics, which reduces the cracking probability. At the same time, the presence of crystals causes crack deflection and crack bridging phenomena, enhancing the fracture toughness. In addition, heat-treatment also leads to an increase in the network connectivity of the glass ceramics, contributing to the improvement of its overall mechanical properties.

1. Introduction

Addressing the inherent brittleness and low fracture toughness of oxide glasses remains a major challenge. It constrains the use of glass in many applications, such as electronic processing, information transmission, and medical device manufacturing [1,2]. The emergence of glass-ceramics has made up for this shortcoming. Since Stookey at Corning Glass Works discovered glass-ceramics by accident [3], glass-ceramics have been applied as electronic equipment, high-end precision instruments, chemical and mechanical equipment, as well as daily life appliances [4–6]. The excellent mechanical properties of many glass-ceramics are key factors for their commercial success. For example, aluminosilicate glass-ceramics with high fracture resistance have been successfully used in protective cover glass, such as in mobile phone screens [7]. The high flexural strength and fracture toughness of Zr-containing silicate glass-ceramics have also proven their important

value in the field of dental restoration [8,9]. Nevertheless, the presence of crystals in a glass matrix may also reduce its service life. For example, large strains around the crystals in ferroelectric glass-ceramics cause cracks and defects due to the volume changes under an external electric field [10], and in thermal shock-resistant glass-ceramics, the high thermal expansion mismatch and crystal anisotropy of crystals and glass cause spontaneous microcracks [11]. Furthermore, glass-ceramics can be sensitive to stress concentration around cracks, which will reduce their resistance to cracking [12].

Recent research shows that the mechanical and thermal properties of glass-ceramics depend not only on their microstructure and chemical composition, but also on the residual stresses generated by the mismatch of coefficients of thermal expansion (CTE) during the cooling process of the crystals and glass matrix [13]. The distribution of residual stresses can be described by models of residual stresses, including Selsing's model [14], Eshelby's model [15] and Green's model [16]. Based on

these models, the relationship between residual stresses and differences in precipitate sizes, volume fractions, and coefficients of thermal expansion can be explained [17–19]. Studying glass-ceramics with varying CTE of the crystals and glass matrix is important since the relative difference in CTE can cause different modes of crack propagation (through-crystal fracture and along-crystal fracture [20]) and microcracks [21], which in turn may have a significant impact on the mechanical properties. The precipitation of low CTE crystals to produce residual compressive stresses has been reported in different glass-ceramic systems, including Li_2O-Al_2O_3-SiO_2 [22–25], Li_2O-SiO_2 [26], and zinc silicate [27], as well as low CTE droplet phase in phase separated glass [28].

Earlier studies reported that residual stress contributes to the increase in fracture toughness. Taya et al. [21] reported that compressive residual stress is typically found to increase the fracture toughness, with similar toughening mechanisms found in other heterogeneous materials, such as borosilicate glass matrix composite containing alumina platelets [29,30] and phase separated glass [28]. However, more recent work on residual stress in glass and ceramic materials has found that residual stress is not related to changes in fracture toughness [31,32]. Mariana et al. [26] found that the best-case scenario for the effect of residual stress (compressive or tensile) on fracture toughness would be a minimal CTE difference between the crystal and the glass matrix, while a smaller CTE differences would reduce the stored elastic energy available for crack initiation or propagation. However, this is insufficient to significantly improve fracture toughness. Crystals in glass-ceramics tend to increase fracture toughness through crack deflection and crack bridging [33]. Studies on residual stress to improve the surface quality of glasses and glass-ceramics have been widely reported, including chemical strengthening, tempering, and coating methods [34–36]. Compressive stress in glass and glass ceramics can effectively improve the surface strength of the material, such as crack initiation resistance (CR) [22]. Such stress can also be formed due to the precipitation of low CTE crystals. In detail, when the CTE of the precipitated crystals is higher than that of the glass matrix, tensile stresses generated at the glass-crystal interface can provide crack initiation sites [20]. In contrast, the precipitation of crystals with a lower CTE generates homogeneous compressive stresses at the crystal, and compressive radial stresses and tensile tangential stresses in glass matrix, which inhibits crack initiation [37]. Thus, the combination of low-CTE crystals and high-CTE glass matrix is expected to improve the crack initiation resistance.

Al_2O_3, B_2O_3 and SiO_2 are typical network-forming glass components with low CTE. At the same time, alkaline earth oxides can be used to prepare hard and stiff glasses due to their high cationic field strength relative to alkali oxides. Consequently, aluminoborate glass-ceramics containing alkaline earth metal oxides are expected to feature higher modulus and lower CTE compared to silica-based glass-ceramics. The CTE of MgO–B_2O_3–Al_2O_3 type glasses is known to be about 4–$6 \times 10^{-6}/$°C [38], which is lower than other alkaline-earth metal oxide glasses of the same main group [39,40]. In the former glass, $MgAl_2O_4$ crystal with a spinel structure is precipitated in the glass-ceramics as the primary phase and reacts with B_2O_3 at high temperature to form a low CTE aluminoborate crystal phase ($Al_4B_2O_9$) and a high mechanical strength crystal phase ($Mg_2B_2O_5$) [41]. However, the mechanical properties of MgO-B_2O_3-Al_2O_3 glass-ceramics have not yet been studied in detail, especially fracture toughness and crack initiation resistance. Most of the proposed applications of MgO-B_2O_3-Al_2O_3 glass-ceramics are within semiconductors and signal transmission, and therefore, it is indeed important to study the mechanical properties of this system.

In general, the fracture toughness of boroaluminate glass is lower than that of silicate glass (because of the high bond energy of Si-O), but boroaluminate glass shows higher crack resistance. Ke et al. [42] have found that in magnesium aluminosilicate glass-ceramics, the self-adaptation ability of MgO and Al_2O_3 can achieve stress dissipation by changing their coordination environment, which is similar to the view of other studies that CR is related to densification capacity [43].

Moreover, the pores formed between the crystalline phase and the residual glass phase, as well as crack deflection, multiple cracking, and crack bridging phenomena, can effectively increase the fracture toughness of glass-ceramics [33]. Therefore, it is interesting to introduce low CTE crystals into glass to increase both CR and fracture toughness of glass-ceramics.

In this work, we therefore design glass-ceramics with an aluminoborate glass network and high field strength Mg^{2+} as the network "modifier". Compared with other alkaline earth modifiers, MgO as a modifier can produce more and higher coordinated Al and B in the glass-ceramic structure [43], which can enhance the mechanical properties of the glass-ceramics. We include Nb_2O_5 as a nucleating agent based on its ability to reduce the nucleation kinetics barrier, increase the nucleation rate, and increase the network connectivity [44,45]. Based on our recent work [46], we therefore here prepare a glass with composition of $23MgO$-$18.4Al_2O_3$-$50.6B_2O_3$-$8Nb_2O_5$ (mol%) by the melt-quenching method. The crystallinity of the glass-ceramics is adjusted by heat-treatment for different durations, and the resulting atomic-scale structures are analyzed by solid-state nuclear magnetic resonance (NMR) and Raman spectroscopy to establish a link with mechanical properties such as fracture toughness and crack initiation resistance.

2. Experiment details

2.1. Sample Preparation

The glass with a composition of $23MgO$-$18.4Al_2O_3$-$50.6B_2O_3$-$8Nb_2O_5$ (mol%) was prepared by conventional melt-quenching method. We added the raw materials $MgCO_3$ (≥ 98 %, Sigma-Aldrich), Al_2O_3 (≥ 99.99 %, Sigma-Aldrich), H_3BO_3 (≥ 99.5 %, Sigma-Aldrich) and Nb_2O_5 (≥ 99.9 %, Sigma-Aldrich)) into a PtRh crucible and homogenized the melt at 1400 °C for 1 h, and then performed quenching by pouring it onto a Cu plate. To obtain a more homogeneous glass, we crushed the obtained glass and performed a second melt-quenching under the same experimental conditions. Following the approach of Li et al. [47], we analyzed the chemical composition (mol%) of the prepared glass using inductively coupled plasma optical emission spectrometry (ICP-OES). The test results showed that the composition is $22.1MgO$-$17.8Al_2O_3$-$52.4B_2O_3$-$7.8Nb_2O_5$, i.e., similar to that of the nominal composition.

After melt-quenching, the obtained glass was quickly transferred to a preheated annealing furnace and annealed for 30 min at the predicted T_g temperature, followed by re-annealing for 30 min at the measured actual T_g temperature (see Section 2.2). Subsequently, these samples were cut into $10 \times 10 \times 3$ mm³ blocks for heat-treatment. According to the DSC curve (Supporting Figure S1), the temperature at which the crystallization started was selected as the temperature of the heat-treatment (680 °C). In detail, the glass was heat treated for 4, 8, 12, and 16 h at 680 °C to prepare glass-ceramics (named as MABN-0, MABN-4, MABN-8, MABN-12 and MABN-16, respectively). After cooling, the glass-ceramics samples were polished in ethanol with SiC sandpaper (240–4000 grit) for subsequent testing.

2.2. Basic property characterization

The glass transition temperature (T_g) was measured using differential scanning calorimetry (DSC) (STA 449 F1, Netzsch). A small sample of ~40 mg weight was heated in a Pt crucible under argon flow (gas flow rate of 40 mL min⁻¹) to 800 °C at a heating rate of 10 K/min, and then cooled to room temperature at 40 K min⁻¹. T_g was considered as the intercept between the tangent to the inflection point of the heat absorption peak and the extrapolated heat flow (Supporting Figure S1).

The transmittance of the precursor glass and glass-ceramic samples was tested using UV–visible spectroscopy (Cary 50 Bio, Varian). The measurements were performed in the visible range of 400–800 nm with a scanning speed of 60 nm/min. Every sample was tested three times and

the final spectral data were normalized to a thickness of 1 mm.

The coefficient of thermal expansion (CTE) of glass and glass-ceramics was tested using a dilatometer (DIL402C, Netzsch) in an Ar atmosphere (gas flow rate of 50 mL min^{-1}). The samples were cut into $3 \times 3 \times 10$ mm^3 rectangles and heated at 2 °C/min to 680 °C. The CTE of the samples was calculated from the slopes of the curves in the temperature range of 100–600 °C.

2.3. Structural characterization

The morphology of crystals and induced damage in the glass-ceramics was observed using field emission scanning electron microscopy (SEM) on polished samples. These polished samples were etched with 10 vol% HF for 5 s for crystal morphology observation (figures shown in the main part of this work) and etched with 10 vol% HF for 10 s for crystal distribution observation (figures shown in the supporting information). The samples used for indentation morphology test were not etched. To improve the electrical conductivity, the samples were sprayed with gold (in the case of all SEM images shown in the main part of this work), or coated with 10 nm platinum (in the case of all SEM images shown in the supporting information). SEM images shown in the main part of this work were acquired using a Zeiss EVO 60 field emission SEM operated at a voltage of 15 kV. A Tescan Clara UHR SEM was used for the acquiring of SEM images shown in the supporting information. The instrument was operated at a voltage of 5 keV and a beam current of 300 pA in UH-resolution scan mode with the potential tube mode set to bright beam. A working distance of around 10 cm was used. Images were acquired with an Everhart-Thornley type (YAG Crystal) detector.

The crystalline phases in the glass-ceramics were analyzed by the Empyrean PANalytical X-ray diffractometer using Cu-Kα1 radiation (1.5405 Å). The polished samples were placed on a carrier stage and scanned in the 5–75° range at a scan rate of 1.75 ° min^{-1} under operating conditions of 40 kV and 20 mA. To estimate the crystallinity, JADE 6.0 software was used to fit the diffraction peak of crystals.

Raman spectra were collected using a micro-Raman spectrometer (inVia, Renishaw). Sample surfaces were excited by a 532 nm diode pumped solid state laser. Spectra were scanned over a range of 200–1600 cm^{-1} with a resolution of > 2 cm^{-1}. At least three different positions were detected for each sample to ensure homogeneity. All spectra were subsequently background corrected and area normalized in Origin software.

Solid-state ^{11}B and ^{27}Al magic angle spinning (MAS) NMR spectroscopy was used to characterize the short-range structure of the samples. The measurements were performed at a magnetic field of 16.4 T using a commercial spectrometer (VNMRS, Agilent) and a commercial 3.2 mm MAS NMR probe (Agilent). Glass and glass-ceramics were ground into powder with a mortar and pestle and then loaded into a 3.2 mm diameter zirconia rotor, and the samples were spun for ^{11}B and ^{27}Al MAS NMR at 20 and 22 kHz, respectively. The resonance frequencies of ^{11}B and ^{27}Al are 224.52 and 182.3 MHz, respectively, and the data for both nuclei were obtained using a short radio-frequency (RF) pulse width of 0.6 μs (π/12 tip angle) with recovery delays of 5 and 2 s, respectively. 600–1000 scans were performed for signal averaging in each experiment. The MAS NMR spectra of ^{11}B and ^{27}Al were plotted using the normal shielding convention, with an aqueous solution of boric acid (19.6 ppm) and an aqueous solution of aluminum nitrate (0.0 ppm), respectively, as the NMR shift reference. The collected data were fitted using DMFit [48]. We used second-order quadrupole lineshapes to fit the resonances of B^{III} units, and used a combination of Gaussian and Lorentz functions to fit the resonance of B^{IV} unit. ^{27}Al MAS NMR data were fitted using the CzSimple model, accounting for distributions in quadrupolar coupling.

^{93}Nb MAS NMR spectra were collected at 16.4 T (171.04 MHz resonance frequency) using a 3.2 mm MAS NMR probe and sample was rotated at 20.0 kHz. A rotor-synchronized Hahn-echo sequence, with rf pulses of 1 and 2 μs, an echo delay of 50 μs, and recycle delays of 2 s were used to collect 10,000–20,000 scans. Data were Fourier transformed after shifting the time domain signal to the echo maximum, without additional apodization. Spectra were referenced using the IUPAC convention with ^{27}Al of aqueous aluminum nitrate at 0.0 ppm [49,50]. ^{93}Nb MAS NMR data were fitted using the Czjzek function in DMFit.

2.4. Mechanical properties

The density of each sample was measured using the Archimedes' principle. Every sample was measured ten times each in air and anhydrous ethanol ($\rho = 0.791$ g/cm^3). The elastic moduli were measured using an ultrasonic thickness gauge (38DL Plus, Olympus) based on the pulse-echo method. 20 MHz piezoelectric transducers were used to generate transverse acoustic waves (V_T) and longitudinal acoustic waves (V_L). The longitudinal modulus (C_{11}), Young's modulus (E), shear modulus (G), bulk modulus (K), and Poisson's ratio (v) were then calculated based on the measured densities,

$$C_{11} = \rho V_L^2 \tag{1}$$

$$G = \rho V_T^2 \tag{2}$$

$$K = C_{11} - \frac{4}{3}G \tag{3}$$

$$v = \frac{3K - 2G}{6K + 2G} \tag{4}$$

$$E = 2G + 2Gv \tag{5}$$

The Vickers hardness (H_V) and crack initiation resistance (CR) of the samples were measured utilizing a micro indentation tester (Nanovea CB500). To measure hardness, 15 indentations were made using the Vickers 136° diamond indenter with a load of 0.98 N at a loading rate of 9.8 N min^{-1} and a holding time of 15 s. To measure the crack resistance (CR), we counted the number of corner cracks emerging after Vickers indentation at varying loads. Counting was done 24 h after indentation under laboratory conditions at room temperature and relative humidity of 45–50 %. CR was then determined as the load at which the crack probability is 50 %. Each polished sample was subjected to 15 indentation tests at different loads with a holding time of 6 s. The possibility of cracking was calculated at each load, and the CR value was determined by plotting a curve using Logistic fitting.

The fracture toughness (K_{Ic}) of the samples was tested using the single-edge pre-cracked beam (SEPB) method. All the polished samples were prepared as $1.5 \times 2 \times 10$ mm^3 beams, following the approach described and validated in our recent work [51]. On these samples, we introduced a line of Vickers indents in the middle of the breadth side ($B = 1.5$ mm) of the sample, with a load of 9.8 N for a dwell time of 10 s. Then, the side with the Vickers indents was placed face down in a bridge compression fixture [52,53]. A load was applied to the sample with a universal testing machine (Z100, Zwick) at a loading rate of 0.05 mm min^{-1}, which resulted in the growth and joining of cracks at the corners of the Vickers indents and eventually expanding to half of the width of the specimen, ending up with a pre-crack length of ∼0.5 W (W is the width of the beam; here $W = 2$ mm). Next, the samples with pre-cracks were placed in a three-point bending fixture, and the specimens were loaded to fracture at a crosshead speed of 0.9 mm min^{-1} using the same universal testing machine. The fractured samples were collected after the test and the length of the pre-cracks, a, was measured using an optical microscope. We used a three-point bending set-up with a support span (S) of 8 mm to achieve a span ratio (S/W) of ∼4. It should be noted that this ratio may be different for beams with different sizes. The peak load, P_{max}, during loading was used to calculate the fracture toughness,

$$K_{Ic} = \frac{P_{max}}{B\sqrt{W}} Y^* \qquad (6)$$

$$Y^* = \frac{3S}{2W} \frac{\sqrt{\alpha}}{\sqrt[2]{(1-\alpha)^3}} f(\alpha) \qquad (7)$$

where α is the ratio of pre-crack to width (a/W, $a = (a_1 + a_2 + a_3) / 3$), f$(\alpha) = [1.99 - (\alpha - \alpha^2) \times (2.15 - 3.93\alpha + 2.7\alpha^2)]/(1 + 2\alpha)$. The fracture toughness was taken as the average of five measurements for each sample.

2.5. DFT simulations

To obtain knowledge of the CTE of the crystals in the glass-ceramics, we performed density functional theory (DFT) calculations on $Al_2B_4O_9$ and Nb_2O_5 crystals based on the projector augmented wave (PAW) method [54,55]. The initial structures were obtained from the Materials Project database [56]. The simulations were done using the Vienna ab initio simulation package (VASP) [57], which uses a generalized gradient approximation scheme in the form of Perdew Burke-Ernzerhof (PBE) to describe the electronic interaction correlation function [58]. Using $3 \times 3 \times 3$ Monkhorst-Pack k-mesh to collect data on the electron Bloch wave function [59,60], the energy cutoff for the plane-wave basis set was 600 eV. The lattice parameters and internal atomic coordinates were fully relaxed using a convergence criterion of a total energy of $1.0 \cdot 10^{-6}$ eV atom^{-1}. Phonon calculations for the crystals were performed using the finite displacement method described in the PHONOPY software package [61]. Density-functional perturbation theory (DFPT) implemented in the VASP code evaluates the force constants between atoms and calculates the phonon frequencies from the force constants.

For the two crystals present in the glass-ceramic samples, we constructed an $Al_2B_4O_9$ unit cell (120 atoms, monoclinic) and a $1 \times 2 \times 2$ Nb_2O_5 supercell (56 atoms, monoclinic), respectively. Then, we calculated the Helmholtz free energy and thermal properties with a finite displacement (FD) of 0.01 Å to prevent fictitious interactions. The CTE of the crystal was calculated using the quasi-harmonic approximation (QHA) and Grüneisen theory [59]. In detail, 11 crystals with different scaling structures were established based on the volume of the equilibrium structure crystal ($\Delta V/V = \pm 5$ % with a step size of 1 %). Finally, the minimum free energy corresponding to the equilibrium

volume at finite temperature was obtained by fitting the third-order Birch-Murnaghan equation of state (EOS) [62]. By repeated testing at different temperatures, the volumetric thermal expansion coefficient was obtained as,

$$\alpha_v(T) = \frac{1}{V} * \left(\frac{\partial V}{\partial T} \right)_P \qquad (8)$$

where T is temperature, V is volume, and P represents the temperature derivative at constant pressure.

3. Result and discussion

3.1. Structure of precursor glass and glass-ceramics

First, we consider the microstructure of the glass-ceramics by comparing the surface morphology of MABN-0 and MABN-16 samples. As shown in Fig. 1a, the MABN-0 sample without heat-treatment is homogeneous and has no obvious signs of crystallization or phase separation (only polishing traces are visible). In the MABN-16 sample, crystal precipitates are observed (Fig. 1b), and when magnified, the morphology of the crystals is found to be needle-like strips, with a size between around 250–350 nm and no obvious systematic orientation (Fig. 1c,d). We have also observed the distribution of crystals at lower magnification (Supporting Figure S2). The results show that the crystals could not be easily observed in the MABN-0 and MABN-4 samples, but the crystals (crystal clusters) are evenly distributed in the MABN-8, MABN-12 and MABN-16 samples. As the heat-treatment time increases, the size of the crystal clusters increases, which reduces the transparency of the glass-ceramics (Supporting Figure S3).

Fig. 2a shows the XRD patterns of the precursor glass and various glass-ceramics. We observe a small number of Bragg peaks assigned to Nb_2O_5 crystals in the precursor glass, which may be because the melt homogenization temperature is below the melting point of Nb_2O_5 (1512 °C), i.e., a small amount of Nb_2O_5 remains in the matrix, but this does not significantly affect the transparency of the as-prepared glass. These crystals are likely very small since they could not be observed in the SEM images (Fig. 1a), consistent also with the larger breadth of the Bragg peaks in the diffractogram. In addition, almost no sidebands corresponding to Nb_2O_5 crystals were found in the NMR results, confirming that the content of Nb_2O_5 crystals in the as-prepared glass is very small.
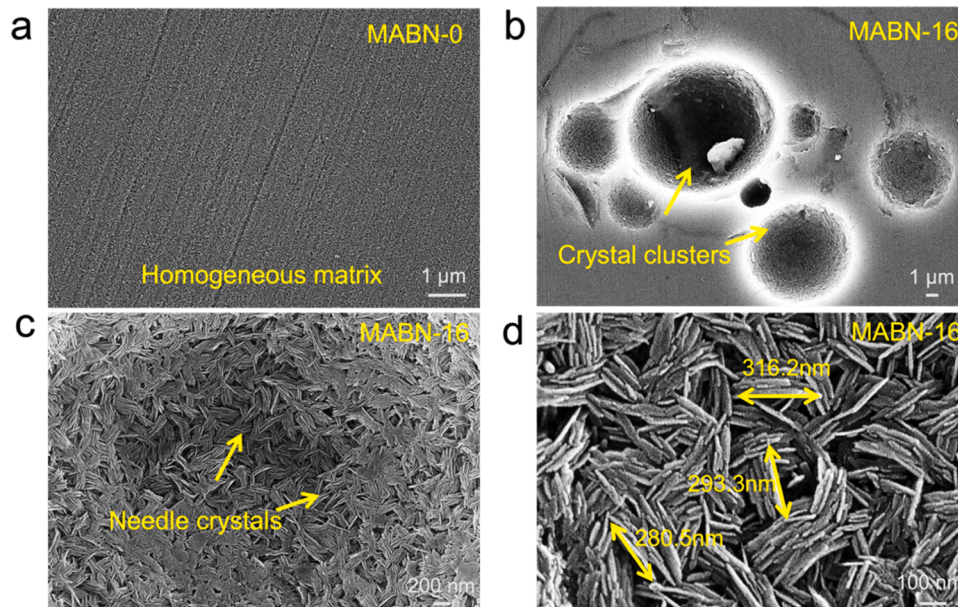

Fig. 1. SEM images of the (a) MABN-0 and (b-d) MABN-16 samples after etching.
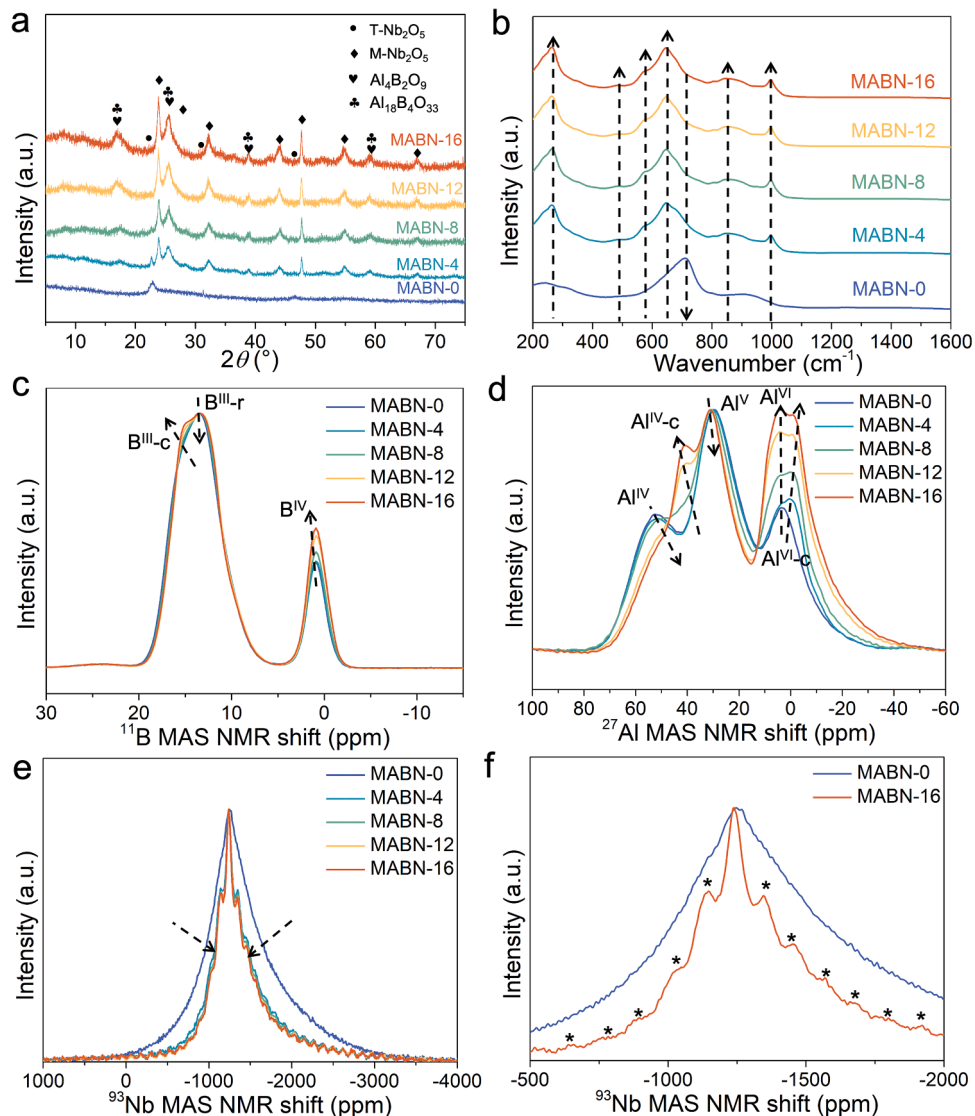
Fig. 2. Structural information of precursor glass and glass-ceramics: (a) XRD, (b) Raman spectroscopy, (c) ^{11}B MAS NMR spectra, and (d) ^{27}Al MAS NMR spectra, (e-f) [93]Nb MAS NMR spectra. Arrows highlight changes in Raman and NMR spectra as the heat treatment time increases. Asterisks in (f) denote spinning sidebands. The powder diffraction file (pdf) numbers of the crystal phases are 30–0873 for T-Nb_2O_5, 19–0862 for M-Nb_2O_5, 09–0158 for $Al_4B_2O_9$, and 29–0009 for $Al_{18}B_4O_{33}$.

With increasing heat-treatment time, the changes in the crystal peak positions are likely due to the phase transition from T-Nb_2O_5 to M-Nb_2O_5 [63], which accompanies some narrowing of the peaks as these crystallites grow in size. Previous work has shown that amorphous niobium oxide (V) begins to crystallize into a "low temperature" form (T-form) at about 773 K, but at higher temperatures up to ~1103 K, there is a transformation from T-Nb_2O_5 to M-Nb_2O_5, with complete conversion achieved by heating at 1273 K for 4 hours [64]. In addition, diffraction peaks due to $Al_4B_2O_9$ and $Al_{18}B_4O_{33}$ crystals appear gradually upon heat-treatment, with the intensity of these peaks increasing with the increase of heat-treatment time. No Mg-containing crystalline phases appeared.

According to the study by Hamzawy et al. [65], aluminoborate phases were formed in glasses with high B_2O_3 content and low MgO and Al_2O_3 contents, which is similar to the present findings. Furthermore, the Mg-containing spinel phase may be formed at an early stage, with element redistribution occurring during the subsequent crystallization process, resulting in MgO remaining in the glass matrix. Reports have shown that $Al_4B_2O_9$ is a sub-stable phase, which can gradually decompose into $Al_{18}B_4O_{33}$ and B_2O_3, and the latter slowly evaporates [66]. However, considering the low heat-treatment temperature in this work,

$Al_4B_2O_9$ is the main crystal phase. We have estimated the crystallinity using JADE software of glass-ceramics, and found it from MABN-0 to MABN-16 samples to be < 1 %, 11.3 %, 16.8 %, 22.9 %, and 30.8 %, respectively. To test for the type of crystallization behavior, we have ground the glass-ceramic samples to different depths (Supporting Figure S4). We find that the XRD patterns of the glass-ceramics obtained after grinding to different depths are almost identical, which suggests that the present glass-ceramics exhibit bulk crystallization.

Raman spectroscopy is used to further analyze the structure of the glass-ceramics (Fig. 2b). The bands in the 200–400 cm^{-1} region can be assigned to the O-Nb-O in the M-Nb_2O_5 octahedron [46,67]. The intensity of the peaks in this region increases with increasing heat-treatment time, which is consistent with the precipitation of Nb_2O_5 crystals detected in the XRD results. The band near 850 cm^{-1} is accompanied by a shoulder near 800 cm^{-1}, which can be attributed to the Nb-O stretching mode NbO_6 unit participating in the Nb-O-Nb connection [68]. The vibration band at ~640 cm^{-1} is attributed to the Nb-O vibration of chained NbO_6 octahedrons [69,70]. These results indicate that Nb participates in the formation of the glass network in the form of NbO_6 octahedrons. The broad band located at ~440–510 cm^{-1} is assigned to the B-O-B bending vibrations [71], and the ~570 cm^{-1}

band is attributed to the O-B-O bending vibrations. The intensities of the peaks within the two regions are slightly increasing upon heat-treatment, which suggests an increased number of B-O-B linkages in the borate glass network, with the presumed partial transition of BO_3 to BO_4 units. Meanwhile, the band representing chain metaborate units (~ 704 cm^{-1}) in the precursor glass disappears upon heat-treatment, while the intensity of the band representing ring metaborate units (~ 644 cm^{-1}) [72] in the glass-ceramics has significantly increased after heat-treatment. The increase in the intensity of the 800–900 cm^{-1} band region is related to the B-O-B units (e.g., chain borate units and B-O-B units present in the boron oxide ring structure), and the 1000 cm^{-1} band are attributed to the B-O-B stretching modes of the BO_4 unit [73,74].

The above results show that the intensities of all the bands associated with tetrahedral B increase after heat-treatment. Likewise, the intensities of the B-O$^-$ associated bands decrease, and the intensities of the bands associated with B-O-B increase in the chained metaborate units. Overall, this suggests an increase in the connectivity of the borate network after heat-treatment. At the same time, the bands in the range 1100–1600 cm^{-1}, corresponding to the B-O$^-$ present in the pyroborate, chain, and ring metaborate units [75], do not change significantly. We also observe an increased network connectivity in the units containing Al atoms. The intensities of peaks corresponding to groups related to the aluminate network increase with the heat-treatment time, such as Al-O$^-$ or Al-O-B (band around 480–500 cm^{-1}) and AlO_4-O-BO_3 groups (bands at ~ 1000 cm^{-1}) [75], and possible Al–O stretching in AlO_6 groups [76]. The above results show that after heat-treatment, the content of highly coordinated B and Al species increases, because the network-formers precipitate from the glass matrix, i.e., the chemical composition of the remaining glass phase changes, e.g., the relative content of Mg atoms in the residual glass phase increases. At the same time, the new AlO_4 and BO_3 groups are attributed to the precipitation of $Al_4B_2O_9$ crystals.

To further investigate the effect of heat-treatment on the short-range structure of the studied glass-ceramics, we have performed solid-state NMR spectroscopy measurements. Fig. 2c,d show the MAS NMR spectra of ^{11}B and ^{27}Al, respectively, with the deconvolution results given in Table 1. The determined speciation and spectral deconvolution are shown in Supporting Figures S5 and S6 and Supporting Tables S1 and S2. We find that the coordination number of B increases upon heat-treatment. The broad peak centered at ~ 14 ppm is assigned to the B^{III} unit, while the peak centered at ~ 1 ppm is assigned to the B^{IV} unit [77]. We further differentiate between two trigonal boron units based on the isotropic chemical shift values (Supporting Figure S5). With increasing heat-treatment time, the ring site trigonal boron (B^{III}-r) tends to transform into a non-ring site (B^{III}-nr), along with the emergence of new B^{III} species, which we attribute to a crystalline trigonal boron environment (B^{III}-c). Combined with the determined quadrupolar coupling constant of 2.57 MHz and quadrupolar asymmetry parameter of 0.16, we find a highly symmetric BO_3 triangle, which corresponds to three-fold coordinated B with all bridging oxygens in the crystal. Earlier work also reports such BO_3 sites in $Al_4B_2O_9$ crystal [78].

Considering the ^{27}Al MAS NMR results (Fig. 2d), the peak centered at ~ 55 ppm is assigned to the Al^{IV} unit, the peak centered at ~ 30 ppm is assigned to the Al^V unit, and the peak centered at ~ 0 ppm is assigned to the Al^{VI} unit. The MABN-0 sample contains the highest fraction of 5-fold coordinated Al, which exceeds the concentrations of Al^{IV} and Al^{VI}. The deconvolution fitting results (Supporting Figure S6) show that with increasing heat-treatment time, the Al^{IV} and Al^V species in the glassy state are partially consumed and converted to Al^{VI}, while new species Al^{IV}-c and Al^{VI}-c are generated due to the precipitation of crystals, which corresponds to the AlO_4 and AlO_6 units in the crystals, respectively. The Al^{IV} deconvolution peak at ~ 38 ppm is very close to the Al^V deconvolution peak, but it is actually an AlO_4 unit (Supporting Figure S7). The phenomenon of transformation of low-coordinated species to higher-coordinated species upon heat-treatment for both B and Al species seems to be related to the precipitation of crystals. Possibly because as $Al_4B_2O_9$ crystals precipitate, the fraction of MgO in the residual glass network increases. Previous research [43] comparing alkaline earth modifiers has shown that the high field strength (FS) of MgO leads to the high coordinated Al and B. This phenomenon has also been observed for other high-FS modifiers (such as La and Y). A possible explanation is that the structural change in glass leads to an increase in the content of "bridging" oxygen bonds with relatively higher negative charges (such as AlO_5-O-BO_4 and AlO_6-O-BO_4, etc.) after crystallization, which high-FS modifier can stabilize more effectively, and thereby promoting the formation of highly coordinated species [79].

Fig. 2e,f show the ^{93}Nb MAS NMR spectra. The Nb in all samples exhibits a 6-coordinated octahedral structure, with the peak centered at approximately -1210 ppm [46,80]. The spectrum of the precursor glass shows a broad, featureless lineshape without any rotational sidebands due to the large quadrupole interaction and its distribution [81]. As the heat treatment time increases, the ^{93}Nb NMR spectra become narrower, reflecting smaller quadrupole interactions due to the ordering and increase in crystalline Nb_2O_5, as seen in XRD. As a consequence of these changes and related narrowing of the ^{93}Nb NMR resonance, a series of shoulder peaks (asterisks in Fig. 2f) appear around the main peak position. These are spaced at the sample spinning frequency and represent satellite transition spinning sidebands for this I= 9/2 nucleus.

Since the ^{93}Nb NMR spectra of heat-treated samples show similar signals, we compared the precursor glass and MABN-16 samples, and the deconvolution results of the two samples are shown in Supporting Figure S8. Deconvolution results show that the average magnitude of the quadrupole coupling constant ($|C_Q|$) of the precursor glass is 68.3 MHz and the Gaussian line broadening (FWHM) is 109 ppm. The isotropic chemical shift is -1200 ppm, which is very similar to the study by Otsuka et al. [82]. The top of the spectrum appears to be narrower than amorphous Nb_2O_5. This may be because the precursor glass contains a small amount of crystalline Nb_2O_5, which is superimposed on this broad and featureless peak. This is consistent with the small amount of Nb_2O_5 peaks in the XRD results.

After heat treatment, the ^{93}Nb MAS NMR deconvoluted spectrum of the MABN-16 sample narrowed significantly and shows many spinning sidebands (Supporting Figure S8a). The appearance of these artifacts and the narrower central transition peak are consistent with niobium crystallizing as Nb_2O_5 (blue peak). When Nb atoms are organized into an ordered/crystalline environment, the line shapes become significantly narrower, reflecting smaller quadrupole interactions. The isotropic chemical shift is approximately -1210 ppm, and the narrow resonance has $|C_Q| = \sim 29$ MHz and FWHM ~ 45 ppm, which is also similar with the literature [68] value for ^{93}Nb in Nb_2O_5.

Finally, we notice that the fitting of the spectrum (dashed line) does not show perfect agreement with the experimental data because the ^{93}Nb MAS NMR deconvolution of MABN-16 appears to be composed not only of the peak and satellite transition sidebands of Nb_2O_5, but also any Nb-containing residual glass phase (Supporting Figure S8b). Although the lineshape indicates narrowing of the ^{93}Nb resonance, consistent with crystallization of Nb_2O_5, the underlying peak is still quite broad and may contain some signal from Nb which remains in the glassy phase (indicated by the broad signal in the orange shaded area), making it difficult

Table 1

Boron and aluminum speciation as determined from deconvolution of the ^{11}B and ^{27}Al MAS NMR spectra. The uncertainty in the area fraction is $\pm$ 0.2 %.

ID	B site			Al site			
	B^{III} Area (%)	B^{IV} Area (%)	Average CN	Al^{IV} Area (%)	Al^V Area (%)	Al^{VI} Area (%)	Average CN
MABN−0	83.8	16.2	3.16	38.7	45.1	16.2	4.77
MABN−4	84.3	15.7	3.16	38.0	43.7	18.3	4.80
MABN−8	83.3	16.7	3.17	43.5	29.3	27.2	4.84
MABN−12	81.5	18.5	3.18	36.8	25.4	37.4	4.99
MABN−16	80.6	19.4	3.19	38.0	20.5	41.5	5.04

to quantify the relative amounts of Nb in the residual glass phase and the crystalline phase.

3.2. Thermal expansion of glass and glass-ceramics

We have calculated the thermal expansion coefficients of the two main crystals ($Al_2B_4O_9$ and Nb_2O_5) that precipitated upon heat-treatment through DFT simulations, due to the difficulty in obtaining experimental CTE data of these crystals. The relationship between the lowest Helmholtz free energy as a function of volume obtained in the state of P = 0 by fitting the Vine state equation is shown in Fig. 3a,b for the two crystals. Then, based on the unit cell volume as a function of temperature (Fig. 3c), the volumetric CTE of the two crystals is calculated as shown in Fig. 3d. We find that the $Al_2B_4O_9$ crystal features slight negative thermal expansion at very low temperatures (~80 K). The volume thermal expansion coefficient increases monotonically with increasing temperature in the temperature range of 80–1000 K, with the simulated CTE at 300 K and 1000 K being 9.89×10^{-6}/K and 11.16×10^{-6}/K, respectively. The volumetric CTE of Nb_2O_5 crystal also increases with the increase of temperature in the range of 80–600 K, but then decreases slightly with temperature above 600 K. The simulated volumetric CTE at 300 K and 1000 K are 7.63×10^{-6}/K and 16.37×10^{-6}/K, respectively. This is similar to the volumetric CTE of Nb_2O_5 crystal reported by Manning et al. [83] of $\sim 11.2 \pm 2.0 \times 10^{-6}$/K (~5.3, 0, and 5.9 $\times 10^{-6}$/K in the a, b, and c directions, respectively) from room temperature to 1000 °C. For isotropic materials, the linear thermal expansion coefficient is 1/3 of the volume expansion coefficient.

We have also tested the CTE of the precursor glass and glass-ceramics experimentally as shown in Supporting Figure S9. The measured volumetric CTE of the precursor glass is 2.22×10^{-5}/K. After heat treatment, the CTE of the glass-ceramics is lower than that of the precursor glass. The MABN-12 sample has the lowest volumetric CTE of 1.94×10^{-5}/K, whereas the CTE of the MABN-16 sample is slightly higher than of the other glass-ceramics, but still below that of the precursor glass. Therefore, as the heat-treatment time increases, the

volumetric CTE decreases. This is interesting as the precipitation of crystals with low CTE will create homogeneous compressive residual stress in the crystals [84,85]. Crystal precipitation changes the composition of the residual glass phase, i.e., when all Al_2O_3 and Nb_2O_5 are precipitated, the residual glass composition is close to MgO-B_2O_3 glass, with an expected volumetric CTE of 1.416–1.503×10^{-5}/K [86]. However, considering the low crystallinity of the present samples, we do not take this CTE difference into account. In addition, all prepared glass-ceramics showed no microcracks caused by the large anisotropy of the CTE of the crystal, which may lead to spontaneous cracking [22].

3.3. Mechanical properties of precursor glass and glass-ceramics

Fig. 4a shows the density and hardness results for the MABN-0 sample, which are 2.78 g/cm^3 and 6.6 GPa, respectively. The density and hardness then increase as crystals grow in the glass with increasing heat-treatment time, reaching values of 2.82 g/cm^3 and 7.1 GPa, respectively, in the MABN-16 sample. Fig. 4b shows the Young's modulus and Poisson's ratio results. We find a pronounced increase in Young's modulus, from 89.3 to 100.8 GPa upon heat-treatment for the longest time. On the other hand, we observe a decrease in the Poisson's ratio after heat-treatment. Fig. 4c shows the crack initiation probability of the samples under different loads, the loads corresponding to the red dashed lines represent the *CR* values for each sample, which are 9.9 N, 8.7 N, 8.6 N, 12.5 N and 12.9 N from sample MABN-0 to sample MABN-16, respectively. Previous reports suggest that when the CTE of the crystals is lower than that of the glass matrix, residual compressive stress will occur in the crystal [13], and a combination of tensile and compressive stresses will be generated in the matrix, which will hinder the generation of cracks. This can be the reason why *CR* increases upon crystallization as discussed in more detail below.

To study the crack growth resistance of the samples, we have used the SEPB method to quantify fracture toughness (Fig. 4d). While the fracture toughness of the precursor glass is 0.62 MPa·m$^{1/2}$, it increases to 0.90 MPa·m$^{1/2}$ for the glass-ceramic with longest heat-treatment time. The higher K_{Ic} of glass-ceramics relative to glasses can generally
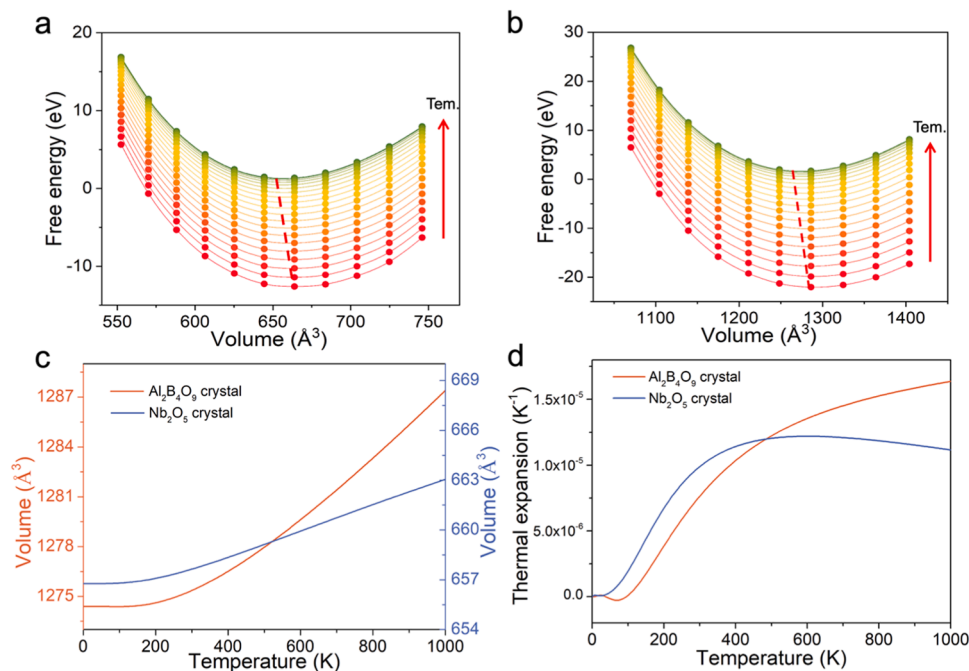

Fig. 3. (a,b) Volume-dependent Helmholtz free energy of (a) Nb_2O_5 crystal and (b) $Al_2B_4O_9$ crystal from 0 K to 2000 K with a step size of 100 K. The solid lines are the fitting curves using the third-order Birch-Murnaghan equation of states, while the dotted lines are the equilibrium volumes determined by the minimum free energy at different temperatures. (c) Temperature dependence of the volume change of Nb_2O_5 and $Al_2B_4O_9$ crystals. (d) Temperature dependence of volumetric coefficients of thermal expansion for Nb_2O_5 and $Al_2B_4O_9$ crystals.
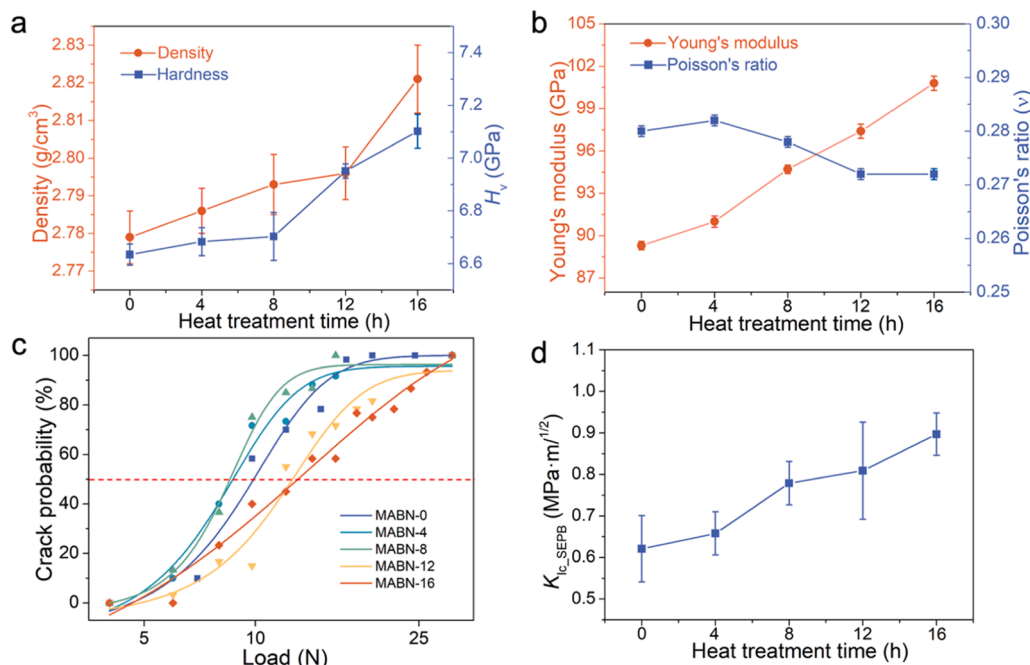
Fig. 4. Mechanical properties of precursor glass and glass-ceramics. (a) Density and Vicker's hardness, (b) Young's modulus and Poisson's ratio, (c) cracking probability as a function of applied indentation loads. and (d) fracture toughness.

be attributed to crack deflection, bridging, and branching during crack growth, thus effectively dissipating highly localized stresses. For example, we have found this in our previous study [46], where K_{Ic} of barium aluminoborate glass-ceramics with ~10 % crystallinity was enhanced by ~41 % over the precursor glass, with evidence of the crystals hindering crack growth. To investigate whether the same phenomenon occurs in the present glass-ceramic samples, we have used SEM to image the crack growth paths due to Vickers indentation. Fig. 5 show the Vickers indentation and crack tip enlargement in the MABN-0 glass, MABN-12 glass-ceramic, and MABN-16 glass-ceramic. In the MABN-0 glass, the indentation produced all straight corner cracks (Fig. 5a,b), and the magnified view of the corner crack shows no crack deflection (region 1). In the MABN-12 and MABN-16 glass-ceramics, the cracks tend to show some straight crack growth and undergo transgranular fracture in the regions close to the indent due to the high intensity of the stress in these region (Fig. 5c and e) [87]. However, the crack tip further away from the indent extends around the crystal grain due to the decrease in crack driving force, which shortens the crack length due to the hindering effect of the crystals, resulting in intergranular fracture. In Fig. 5d, crack deflection can be found near the crystal tip. When further increasing the heat-treatment time, i.e., as crystal size increases, crack bridging can also be seen at the crack tip (Fig. 5f).

We propose that the increase in crack resistance upon crystallization can be ascribed to changes in residual stress and network connectivity. First, residual stresses in glass-ceramics are caused by the CTE mismatch between the crystal and glass matrix phases during the cooling process. A schematic diagram of the residual stress distribution in glass-ceramics due to different CTE is shown in Fig. 6. We assume that the crystals are uniformly distributed in random orientation in the matrix (Fig. 6a). When the CTE of the crystal is lower than that of the glass matrix, the glass matrix will be subjected to average compressive stresses (σ_R) in the radial direction and average tensile stress (σ_T) in the tangential direction (Fig. 6b), while the crystal will be subjected to compressive stress (σ_c) (Fig. 6c). This is because during the cooling process after heat treatment, since the volume change of the crystal with low CTE is smaller than that of the glass matrix, the crystal is subject to compressive stress in all direction. This residual stress distribution has been proved by Selsing's

model [14] and experiments [26,88], and the change in residual stress is positively related to the crystallinity [89]. The combination of tangential tensile stress in glass matrix, crystal size, volume fraction, crystal shape, surface energy, and CTE difference will lead to different crack propagation paths. Cracks can propagate along the crystal-glass interface under the action of tangential tensile stress [90]. The role of tensile stress in promoting crack propagation decreases away from the crystal, which leads to a reduction in crack growth. The radial compressive stress from other crystals will cause the crack tip to be compressed, further hindering the crack propagation. Therefore, glass-ceramics with high crystallinity can introduce more compressive stress, thereby increasing the CR.

Second, improving the network connectivity of glass-ceramics can also help to improve crack resistance and fracture toughness, because crack initiation and propagation requires the breaking of chemical bonds. Although this phenomenon is difficult to observe experimentally, MD simulation work [91–93] has shown that the coordination number of the atoms in the glass network changes under an applied stress, helping to dissipate mechanical energy. Using high field strength Mg^{2+} as modifier can cause an increase in the concentration of AlO_5 units in the glass network [94], which is also confirmed in the NMR result in this work. Then after heat-treatment, the concentration of highly coordinated BO_4 and AlO_6 units increases, which increases the network connectivity of the residual glass phase. This may contribute to improved crack resistance and fracture toughness because the highly coordinated B and Al atoms increase the frequency of bond switching events during the fracture process of glass-ceramics. It should be noted that this increase in network connectivity is different that induced by densification, e.g., through hot compression, which tends to decrease crack resistance [95–99].

4. Conclusion

This work has investigated the structural and mechanical properties of Nb_2O_5 doped magnesium aluminoborate glass-ceramics. The hardness, elastic modulus, and fracture toughness of glass-ceramics are higher than those of the precursor glass. In contrast to most previous work on glass-ceramics, the crack initiation resistance also increases
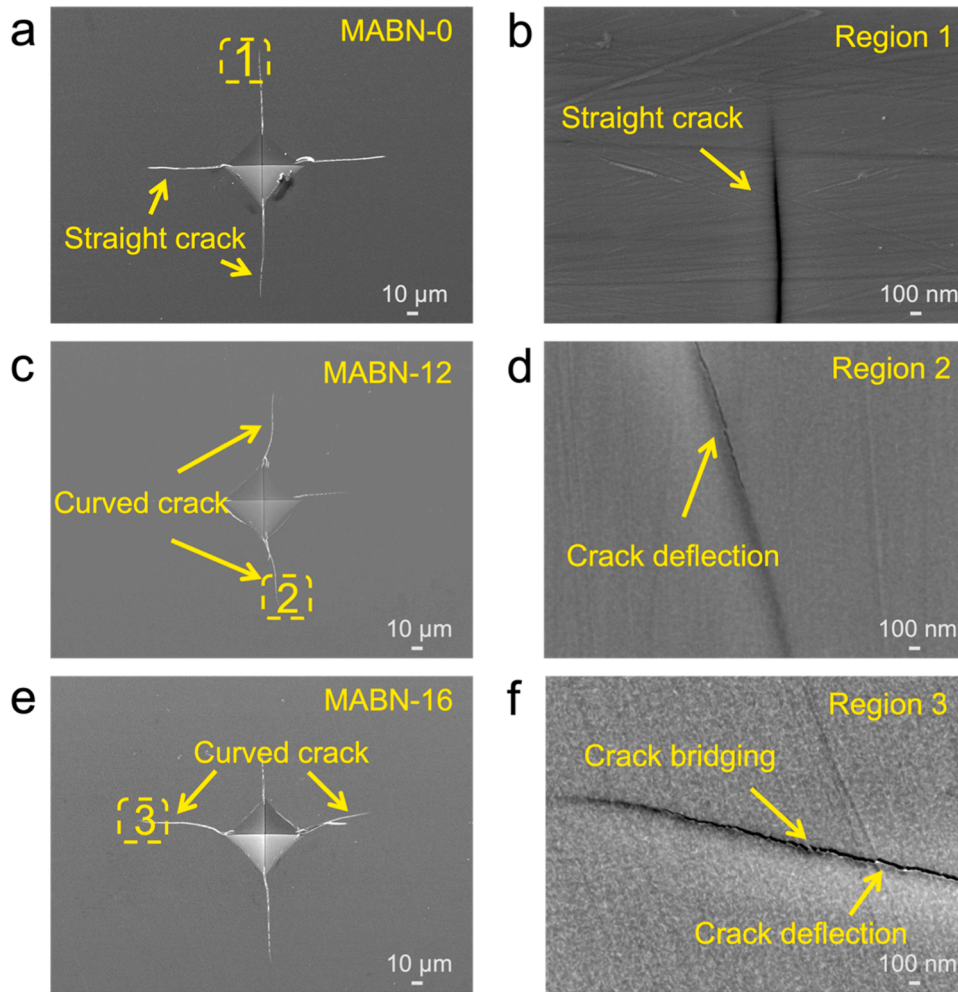
Fig. 5. SEM visualized morphology of indent impression and crack path of (a-b) MABN-0 glass, (c-d) MABN-12 glass-ceramic, and (e-f) MABN-16 glass-ceramic. All indentations were done at a load of 20 N.
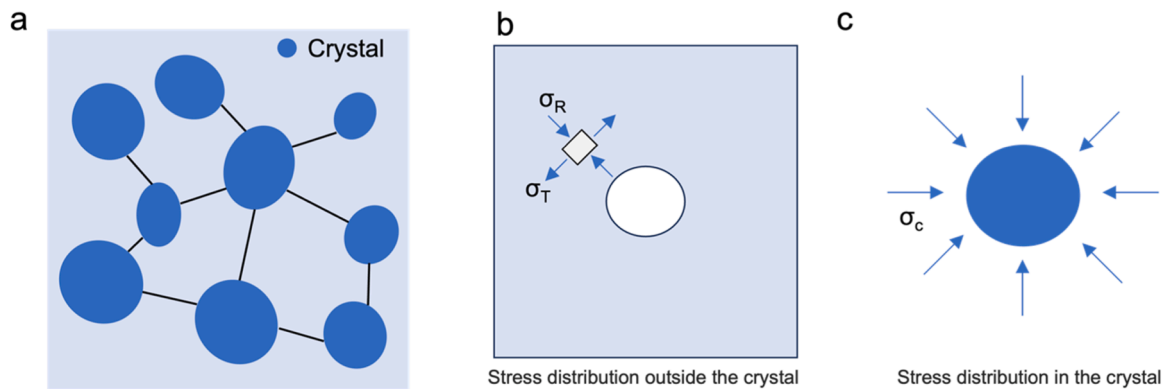

Fig. 6. (a) Schematic diagram of crystal distribution in glass-ceramics. Dark blue circles or ovals represent crystals, light blue area represents the glass matrix, and black lines represent the locations of microcracks in the matrix. Note that such microcracks tend to appear in materials where the thermal expansion of the precipitate is lower than that of the matrix, and the fracture toughness of the precipitate is higher than that of the matrix. Stress distribution (b) outside the crystal and (c) in the crystal when the CTE of the crystal is smaller than that of the matrix, including radial compressive stress and tangential tensile stress in glass matrix and compressive stress in crystal.

with increasing crystal content. We attribute this to the generation of compressive residual stresses in the surface of glass-ceramics after the precipitation of crystals with low coefficient of thermal expansion. However, various factors contribute to the toughening of glass-ceramics. The spherical crystal clusters containing needle-shape crystals can effectively hinder crack propagation, and the increase in the coordination number of B and Al atoms upon crystallization increases the connectivity of the glass network, which likely promotes bond switching events during fracture. This study shows that a combination of high resistance to crack forming and high resistance to crack extension of

glass-ceramics can be achieved by proper composition design of the precursor glass.

CRediT authorship contribution statement

Randall E. Youngman: Writing – review & editing, Investigation, Formal analysis. **Tao Du:** Writing – review & editing, Investigation, Formal analysis. **Qi Zhang:** Writing – review & editing, Investigation. **Daming Sun:** Writing – original draft, Investigation, Formal analysis, Conceptualization. **Morten M Smedskjaer:** Writing – original draft, Supervision, Conceptualization. **Rebekka Klemmt:** Writing – review & editing, Investigation. **Feng Yang:** Writing – review & editing, Investigation. **Deyong Wang:** Writing – review & editing, Investigation. **Lars R. Jensen:** Writing – review & editing, Investigation.

Declaration of Competing Interest

The authors declare that they have no known competing financial interests or personal relationships that could have appeared to influence the work reported in this paper.

Acknowledgements

Conflicts of interest

There are no conflicts to declare.

Appendix A. Supporting information

Supplementary data associated with this article can be found in the online version at doi:10.1016/j.jeurceramsoc.2025.117226.

References

[1] M.S. Shaikh, M.A. Fareed, M.S. Zafar, Bioactive glass applications in different periodontal lesions: a narrative review, Coatings 13 (2023) 716, https://doi.org/10.3390/coatings13040716.

[2] S.H. Choi, S.B. Kwon, J.H. Yoo, M. Na, B.Y. Kim, H. Yoon, S.H. Park, I. Kinski, B. K. Kang, D.H. Yoon, Y.H. Song, Fabrication of phosphor in glass using waste glass for automotive lighting application, Sci. Rep. 13 (2023) 4456, https://doi.org/10.1038/s41598-023-27685-2.

[3] S.D. Stookey, Catalyzed crystallization of glass in theory and practice, Ind. Eng. Chem. 51 (1959) 805–808, https://doi.org/10.1021/ie50595a022.

[4] E.D. Zanotto, A bright future for glass-ceramics, Am. Ceram. Soc. Bull. 89 (8) (2010) 19–27.

[5] Q. Fu, G.H. Beall, C.M. Smith, J.T. Kohli, R.E. Youngman, B.R. Wheaton, A. J. Credle, O. Gulbiten, Strong, tough glass-ceramics for emerging markets, Int. J. Appl. Glass Sci. 7 (2016) 486–491, https://doi.org/10.1111/ijag.12247.

[6] P.F. James, Glass ceramics: new compositions and uses, J. Non-Cryst. Solids 181 (1995) 1–15, https://doi.org/10.1016/0022-3093(94)00515-X.

[7] M.C. Onbaşlı, A. Tandia, J.C. Mauro, Mechanical and compositional design of high-strength corning gorilla® glass, in: W. Andreoni, S. Yip (Eds.), Handbook of Materials Modeling, Springer International Publishing, Cham, 2020, pp. 1997–2019, https://doi.org/10.1007/978-3-319-44680-6_100.

[8] M. Schweiger, M. Frank, S.C.V. Clausbruch, W.H. Land, V. Rheinberger, Microstructure and properties of a composite system for dental applications composed of glass-ceramics in the SiO$_2$–Li$_2$O–ZrO$_2$–P$_2$O$_5$ system and ZrO$_2$-ceramic (TZP), J. Mater. Sci. 34 (1999) 4563–4572, https://doi.org/10.1023/A:1004661911158.

[9] M. Montazerian, E.D. Zanotto, Bioactive and inert dental glass-ceramics, J. Biomed. Mater. Res. A 105 (2017) 619–639, https://doi.org/10.1002/jbm.a.35923.

[10] S. Liu, B. Shen, H. Hao, J. Zhai, Glass–ceramic dielectric materials with high energy density and ultra-fast discharge speed for high power energy storage applications, J. Mater. Chem. C 7 (2019) 15118–15135, https://doi.org/10.1039/C9TC05253D.

[11] R. Benavente, M.D. Salvador, A. Martínez-Amesti, A. Fernández, A. Borrell, Effect of sintering technology in β-eucryptite ceramics: influence on fatigue life and effect of microcracks, Mater. Sci. Eng. A 651 (2016) 668–674, https://doi.org/10.1016/j.msea.2015.11.013.

[12] H. Xie, K. Zhou, S. Hu, J. Fu, S. Duo, J. Shi, Enhancement of damage resistance of transparent Li$_2$O-Al$_2$O$_3$-B$_2$O$_3$ glass by crystallization, J. Non-Cryst. Solids 631 (2024) 122911, https://doi.org/10.1016/j.jnoncrysol.2024.122911.

[13] F.C. Serbena, E.D. Zanotto, Internal residual stresses in glass-ceramics: a review, J. Non-Cryst. Solids 358 (2012) 975–984, https://doi.org/10.1016/j.jnoncrysol.2012.01.040.

[14] J. Selsing, Internal stresses in ceramics, 419–419, J. Am. Ceram. Soc. 44 (1961), https://doi.org/10.1111/j.1151-2916.1961.tb15475.x.

[15] J.D. Eshelby, The determination of the elastic field of an ellipsoidal inclusion, and related problems, Proc. R. Soc. Lond. A 241 (1957) 376–396, https://doi.org/10.1098/rspa.1957.0133.

[16] D.J. Green, Stress-induced microcracking at second-phase inclusions, J. Am. Ceram. Soc. 64 (1981) 138–141, https://doi.org/10.1111/j.1151-2916.1981.tb10244.x.

[17] F.C. Serbena, V.O. Soares, O. Peitl, H. Pinto, R. Muccillo, E.D. Zanotto, Internal residual stresses in sintered and commercial low expansion Li$_2$O-Al$_2$O$_3$-SiO$_2$ glass-ceramics: internal residual stresses in las glass-ceramics, J. Am. Ceram. Soc. 94 (2011) 1206–1214, https://doi.org/10.1111/j.1551-2916.2010.04220.x.

[18] R.I. Todd, B. Derby, Thermal stress induced microcracking in alumina–20% SiCp composites, Acta Mater. 52 (2004) 1621–1629, https://doi.org/10.1016/j.actamat.2003.12.007.

[19] V. Deshpande, A. Evans, Inelastic deformation and energy dissipation in ceramics: a mechanism-based constitutive model, J. Mech. Phys. Solids 56 (2008) 3077–3100, https://doi.org/10.1016/j.jmps.2008.05.002.

[20] R.W. Davidge, T.J. Green, The strength of two-phase ceramic/glass materials, J. Mater. Sci. 3 (1968) 629–634, https://doi.org/10.1007/BF00757910.

[21] M. Taya, S. Hayashi, A.S. Kobayashi, H.S. Yoon, Toughening of a particulate-reinforced ceramic-matrix composite by thermal residual stress, J. Am. Ceram. Soc. 73 (1990) 1382–1391, https://doi.org/10.1111/j.1151-2916.1990.tb05209.x.

[22] J. Yang, J. Xing, Q. Zheng, A. Qiao, H. Tao, Transparent surface crystallized aluminosilicate glasses with an ultrahigh crack resistance, J. Non-Cryst. Solids 635 (2024) 122996, https://doi.org/10.1016/j.jnoncrysol.2024.122996.

[23] M. Kang, W. Li, A.F.T. Leong, M. Guan, K. Fezzaa, J.T. Harris, K.T. Ramesh, T. C. Hufnagel, Crack nucleation and growth during dynamic indentation of chemically-strengthened glass, Extrem. Mech. Lett. 38 (2020) 100754, https://doi.org/10.1016/j.eml.2020.100754.

[24] D.C.N. Fabris, E.H. Miguel, R. Vargas, R.B. Canto, M.D.O.C. Villas-Boas, O. Peitl, V. M. Sglavo, E.D. Zanotto, Microstructure, residual stresses, and mechanical performance of surface crystallized translucent glass-ceramics, J. Eur. Ceram. Soc. 42 (2022) 4631–4642, https://doi.org/10.1016/j.jeurceramsoc.2022.04.024.

[25] E. Kleebusch, C. Thieme, C. Patzig, T. Höche, C. Rüssel, Crystallization of lithium aluminosilicate and microstructure of a lithium alumino borosilicate glass designed for zero thermal expansion, Ceram. Int. 49 (2023) 21246–21254, https://doi.org/10.1016/j.ceramint.2023.03.254.

[26] M.O.C. Villas-Boas, F.C. Serbena, V.O. Soares, I. Mathias, E.D. Zanotto, Residual stress effect on the fracture toughness of lithium disilicate glass-ceramics, J. Am. Ceram. Soc. 103 (2020) 465–479, https://doi.org/10.1111/jace.16664.

[27] C. Bocker, C. Funke, C. Rüssel, Strengthening of a zinc silicate glass by surface crystallization, Mater. Lett. 207 (2017) 41–43, https://doi.org/10.1016/j.matlet.2017.07.045.

[28] J. Häßler, C. Rüssel, Effect of microstructure of a phase separated sodium-borosilicate glass on mechanical properties, Ceram. Int. 43 (2017) 11403–11409, https://doi.org/10.1016/j.ceramint.2017.05.349.

[29] R.I. Todd, A.R. Boccaccini, R. Sinclair, R.B. Yallee, R.J. Young, Thermal residual stresses and their toughening effect in Al$_2$O$_3$ platelet reinforced glass, Acta Mater. 47 (1999) 3233–3240, https://doi.org/10.1016/S1359-6454(99)00177-9.

[30] M. Kotoul, J. Pokluda, P. Šandera, I. Dlouhý, Z. Chlup, A.R. Boccaccini, Toughening effects quantification in glass matrix composite reinforced by alumina platelets, Acta Mater. 56 (2008) 2908–2918, https://doi.org/10.1016/j.actamat.2008.02.024.

[31] F.C. Serbena, I. Mathias, C.E. Foerster, E.D. Zanotto, Crystallization toughening of a model glass-ceramic, Acta Mater. 86 (2015) 216–228, https://doi.org/10.1016/j.actamat.2014.12.007.

[32] L. Fu, H. Engqvist, W. Xia, Glass–ceramics in dentistry: a review, Materials 13 (2020) 1049, https://doi.org/10.3390/ma13051049.

[33] K.T. Faber, A.G. Evans, Crack deflection processes—I. Theory, Acta Metall. 31 (1983) 565–576, https://doi.org/10.1016/0001-6160(83)90046-9.

[34] N. Sheth, A. Howzen, A. Campbell, S. Spengler, H. Liu, C.G. Pantano, S.H. Kim, Effects of tempering and heat strengthening on hardness, indentation fracture resistance, and wear of soda lime float glass, Int. J. Appl. Glass Sci. 10 (2019) 431–440, https://doi.org/10.1111/ijag.13507.

[35] J. Malzbender, G. de With, Cracking and residual stress in hybrid coatings on float glass, Thin. Solid. Films. 359 (2) (2000) 210–214.

[36] D.J. Green, R. Tandon, V.M. Sglavo, Crack arrest and multiple cracking in glass through the use of designed residual stress profiles, Science 283 (1999) 1295–1297, https://doi.org/10.1126/science.283.5406.1295.

[37] J. Selsing, Internal stress in ceramics, J. Am. Ceram. Soc. 44 (1961) 419.

[38] M. Okamoto, H. Kodama, K. Shinozaki, Effect of crystallized phase on mechanical strength of hot-pressed composites of MgO-B$_2$O$_3$-Al$_2$O$_3$ type glass and Al$_2$O$_3$ filler, J. Ceram. Soc. Jpn. 116 (2008) 475–480, https://doi.org/10.2109/jcersj2.116.475.

[39] M.M. Smedskjaer, R.E. Youngman, J.C. Mauro, Impact of ZnO on the structure and properties of sodium aluminosilicate glasses: comparison with alkaline earth

oxides, J. Non-Cryst. Solids 381 (2013) 58–64, https://doi.org/10.1016/j.jnoncrysol.2013.09.019.

[40] M.M. Smedskjaer, J.C. Mauro, J. Kjeldsen, Y. Yue, Microscopic origins of compositional trends in aluminosilicate glass properties, J. Am. Ceram. Soc. 96 (2013) 1436–1443, https://doi.org/10.1111/jace.12298.

[41] E.M.A. Hamzawy, H. Darwish, Vitrification and devitrification phenomena in the ternary MgO–Al_2O_3–B_2O_3 system, Ceram. Int. 34 (2008) 1965–1969, https://doi.org/10.1016/j.ceramint.2007.07.015.

[42] X. Ke, Z. Shan, Z. Li, Y. Tao, Y. Yue, H. Tao, Toward hard and highly crack resistant magnesium aluminosilicate glasses and transparent glass-ceramics, J. Am. Ceram. Soc. 103 (2020) 3600–3609, https://doi.org/10.1111/jace.17048.

[43] K.F. Frederiksen, K. Januchta, N. Mascaraque, R.E. Youngman, M. Bauchy, S. J. Rzoska, M. Bockowski, M.M. Smedskjaer, Structural compromise between high hardness and crack resistance in aluminoborate glasses, J. Phys. Chem. B 122 (2018) 6287–6295, https://doi.org/10.1021/acs.jpcb.8b02905.

[44] A.V. DeCeanne, L.R. Rodrigues, C.J. Wilkinson, J.C. Mauro, E.D. Zanotto, Examining the role of nucleating agents within glass-ceramic systems, J. Non-Cryst. Solids 591 (2022) 121714, https://doi.org/10.1016/j.jnoncrysol.2022.121714.

[45] Q. Zhang, K. Chen, D. Tang, T. Zhang, S.P. Jiang, Effects of Nb_2O_5 and Gd_2O_3 doping on boron volatility and activity between glass seals and lanthanum-containing cathode, J. Eur. Ceram. Soc. 37 (2017) 1547–1555, https://doi.org/10.1016/j.jeurceramsoc.2016.12.007.

[46] Q. Zhang, D. Sun, T. Du, L.R. Jensen, D. Wang, V. Popok, R.E. Youngman, M. M. Smedskjaer, High damage-resistance and fracture toughness of transparent Nb-doped barium aluminoborate glass ceramics, Appl. Mater. Today 34 (2023) 101888, https://doi.org/10.1016/j.apmt.2023.101888.

[47] Z. Li, J. Li, C. Chen, S. Li, J. Hu, J.F.S. Christensen, D. Zhou, L.R. Jensen, J. Ni, X. Qiao, J. Du, M.M. Smedskjaer, K. Shinozaki, Y. Zhang, J. Qiu, J. Ren, Y. Yue, Realizing superior luminescence in oxyfluoride glass-ceramics by enhancing nano-micro phase separation, Adv. Opt. Mater. 12 (2024) 2301999, https://doi.org/10.1002/adom.202301999.

[48] D. Massiot, F. Fayon, M. Capron, I. King, S. Le Calvé, B. Alonso, J. Durand, B. Bujoli, Z. Gan, G. Hoatson, Modelling one- and two-dimensional solid-state NMR spectra, Magn. Reson. Chem. 40 (2002) 70–76, https://doi.org/10.1002/mrc.984.

[49] R.K. Harris, E.D. Becker, R. Goodfellow, P. Granger, NMR nomenclature. Nuclear spin properties and conventions for chemical shifts (IUPAC Recommendations 2001), Pure. Appl. Chem. 73 (2001) 1795–1818, https://doi.org/10.1351/pac200173111795.

[50] R.K. Harris, E.D. Becker, S.M.C. De Menezes, P. Granger, R.E. Hoffman, K.W. Zilm, Further conventions for NMR shielding and chemical shifts (IUPAC recommendations 2008), Solid. State Nucl. Mag. 46 (2008) 582–598, https://doi.org/10.1002/mrc.2225.

[51] T. To, S.S. Sørensen, J.F.S. Christensen, R. Christensen, L.R. Jensen, M. Bockowski, M. Bauchy, M.M. Smedskjaer, Bond switching in densified oxide glass enables record-high fracture toughness, ACS Appl. Mater. Inter. 13 (2021) 17753–17765, https://doi.org/10.1021/acsami.1c00435.

[52] T. To, C. Stabler, E. Ionescu, R. Riedel, F. Célarié, T. Rouxel, Elastic properties and fracture toughness of SiOC-based glass-ceramic nanocomposites, J. Am. Ceram. Soc. 103 (2020) 491–499, https://doi.org/10.1111/jace.16686.

[53] T. To, F. Célarié, C. Roux-Langlois, A. Bazin, Y. Gueguen, H. Orain, M. Le Fur, V. Burgaud, T. Rouxel, Fracture toughness, fracture energy and slow crack growth of glass as investigated by the Single-Edge Precracked Beam (SEPB) and Chevron-Notched Beam (CNB) methods, Acta Mater. 146 (2018) 1–11, https://doi.org/10.1016/j.actamat.2017.11.056.

[54] P.E. Blöchl, Projector augmented-wave method, Phys. Rev. B 50 (1994) 17953–17979, https://doi.org/10.1103/PhysRevB.50.17953.

[55] G. Kresse, D. Joubert, From ultrasoft pseudopotentials to the projector augmented-wave method, Phys. Rev. B 59 (1999) 1758–1775, https://doi.org/10.1103/PhysRevB.59.1758.

[56] A. Jain, S.P. Ong, G. Hautier, W. Chen, W.D. Richards, S. Dacek, S. Cholia, D. Gunter, D. Skinner, G. Ceder, K.A. Persson, Commentary: the materials project: a materials genome approach to accelerating materials innovation, Apl. Mater. 1 (2013) 011002, https://doi.org/10.1063/1.4812323.

[57] G. Kresse, J. Furthmüller, Efficient iterative schemes for *ab initio* total-energy calculations using a plane-wave basis set, Phys. Rev. B 54 (1996) 11169–11186, https://doi.org/10.1103/PhysRevB.54.11169.

[58] J.P. Perdew, K. Burke, M. Ernzerhof, Generalized gradient approximation made simple, Phys. Rev. Lett. 77 (1996) 3865–3868, https://doi.org/10.1103/PhysRevLett.77.3865.

[59] Y. Li, J. Wang, J. Wang, Theoretical investigation of phonon contributions to thermal expansion coefficients for rare earth monosilicates RE_2SiO_5 (RE = Dy, Ho, Er, Tm, Yb and Lu), J. Eur. Ceram. Soc. 40 (2020) 2658–2666, https://doi.org/10.1016/j.jeurceramsoc.2019.09.042.

[60] A. Togo, L. Chaput, I. Tanaka, G. Hug, First-principles phonon calculations of thermal expansion in Ti_3SiC_2, Ti_3AlC_2, and Ti_3GeC_2, Phys. Rev. B 81 (2010) 174301, https://doi.org/10.1103/PhysRevB.81.174301.

[61] A. Togo, F. Oba, I. Tanaka, First-principles calculations of the ferroelastic transition between rutile-type and $CaCl_2$-type SiO_2 at high pressures, Phys. Rev. B 78 (2008) 134106, https://doi.org/10.1103/PhysRevB.78.134106.

[62] F. Birch, Finite elastic strain of cubic crystals, Phys. Rev. 71 (1947) 809–824, https://doi.org/10.1103/PhysRev.71.809.

[63] G.H.D.M. Gomes, R.R.D. Andrade, N.D.S. Mohallem, Investigation of phase transition employing strain mapping in TT- and T-Nb_2O_5 obtained by HRTEM micrographs, Micron 148 (2021) 103112, https://doi.org/10.1016/j.micron.2021.103112.

[64] I. Nowak, M. Ziolek, Niobium compounds: preparation, characterization, and application in heterogeneous catalysis, Chem. Rev. 99 (1999) 3603–3624, https://doi.org/10.1021/cr9800208.

[65] E.M.A. Hamzawy, H. Darwish, Vitrification and devitrification phenomena in the ternary MgO–Al_2O_3–B_2O_3 system, Ceram. Int. 34 (2008) 1965–1969, https://doi.org/10.1016/j.ceramint.2007.07.015.

[66] T. Sun, H. Xiao, Y. Cheng, H. Liu, Effects of MO (MBa, Mg, Ca) on the crystallization of B_2O_3–Al_2O_3–SiO_2 glass-ceramics, Ceram. Int. 35 (2009) 1051–1055, https://doi.org/10.1016/j.ceramint.2008.04.017.

[67] S.M. Hsu, J.J. Wu, S.W. Yung, T.S. Chin, T. Zhang, Y.M. Lee, C.M. Chu, J.Y. Ding, Evaluation of chemical durability, thermal properties and structure characteristics of Nb–Sr-phosphate glasses by Raman and NMR spectroscopy, J. Non-Cryst. Solids 358 (2012) 14–19, https://doi.org/10.1016/j.jnoncrysol.2011.08.006.

[68] H. Bradtmüller, Q. Zheng, A. Gaddam, H. Eckert, E.D. Zanotto, Structural impact of niobium oxide on lithium silicate glasses: results from advanced interaction-selective solid-state nuclear magnetic resonance and Raman spectroscopy, Acta Mater. 255 (2023) 119061, https://doi.org/10.1016/j.actamat.2023.119061.

[69] A. Flambard, J.J. Videau, L. Delevoye, T. Cardinal, C. Labrugère, C.A. Rivero, M. Couzi, L. Montagne, Structure and nonlinear optical properties of sodium–niobium phosphate glasses, J. Non-Cryst. Solids 354 (2008) 3540–3547, https://doi.org/10.1016/j.jnoncrysol.2008.03.017.

[70] H. Maeda, S. Lee, T. Miyajima, A. Obata, K. Ueda, T. Narushima, T. Kasuga, Structure and physicochemical properties of CaO–P_2O_5–Nb_2O_5–Na_2O glasses, J. Non-Cryst. Solids 432 (2016) 60–64, https://doi.org/10.1016/j.jnoncrysol.2015.06.003.

[71] P. Pascuta, R. Lungu, I. Ardelean, FTIR and Raman spectroscopic investigation of some strontium–borate glasses doped with iron ions, J. Mater. Sci Mater. Electron. 21 (2010) 548–553, https://doi.org/10.1007/s10854-009-9955-7.

[72] S.G. Motke, S.P. Yawale, S.S. Yawale, Infrared spectra of zinc doped lead borate glasses, Bull. Mater. Sci. 25 (2002) 75–78, https://doi.org/10.1007/BF02704599.

[73] H. Li, Y. Su, L. Li, D.M. Strachan, Raman spectroscopic study of gadolinium(III) in sodium-aluminoborosilicate glasses, J. Non-Cryst. Solids 292 (2001) 167–176, https://doi.org/10.1016/S0022-3093(01)00878-X.

[74] M. Bengisu, R.K. Brow, E. Yilmaz, A. Moguš-Milanković, S.T. Reis, Aluminoborate and aluminoborosilicate glasses with high chemical durability and the effect of P_2O_5 additions on the properties, J. Non-Cryst. Solids 352 (2006) 3668–3676, https://doi.org/10.1016/j.jnoncrysol.2006.02.118.

[75] R.K. Brow, D.R. Tallant, G.L. Turner, Polyhedral arrangements in lanthanum aluminoborate glasses, J. Am. Ceram. Soc. 80 (2005) 1239–1244, https://doi.org/10.1111/j.1151-2916.1997.tb02970.x.

[76] P. Pernice, S. Esposito, A. Aronne, V.N. Sigaev, Structure and crystallization behavior of glasses in the BaO–B_2O_3–Al_2O_3 system, J. Non-Cryst. Solids 258 (1999) 1–10, https://doi.org/10.1016/S0022-3093(99)00554-2.

[77] T. Edwards, T. Endo, J.H. Walton, S. Sen, Observation of the transition state for pressure-induced $BO_3 \rightarrow BO_4$ conversion in glass, Science 345 (2014) 1027–1029, https://doi.org/10.1126/science.1256224.

[78] K.J.D. MacKenzie, M.E. Smith, T.F. Kemp, D. Voll, Crystalline aluminium borates with the mullite structure: A 11B and 27Al solid-state NMR study, Appl. Magn. Reson 32 (2007) 647–662, https://doi.org/10.1007/s00723-007-0044-x.

[79] S. Bista, E.I. Morin, J.F. Stebbins, Response of complex networks to compression: Ca, La, and Y aluminoborosilicate glasses formed from liquids at 1 to 3 GPa pressures, J. Chem. Phys. 144 (2016) 044502, https://doi.org/10.1063/1.4940691.

[80] O.B. Lapina, D.F. Khabibulin, K.V. Romanenko, Z. Gan, M.G. Zuev, V. N. Krasil'nikov, V.E. Fedorov, 93Nb NMR chemical shift scale for niobia systems, Solid. State Nucl. Mag. 28 (2005) 204–224, https://doi.org/10.1016/j.ssnmr.2005.09.003.

[81] K.O. Drake, D. Carta, L.J. Skipper, F.E. Sowrey, R.J. Newport, M.E. Smith, A multinuclear solid state NMR study of the sol–gel formation of amorphous Nb_2O_5–SiO_2 materials, Solid. State Nucl. Mag. 27 (2005) 28–36, https://doi.org/10.1016/j.ssnmr.2004.08.008.

[82] T. Otsuka, M.R. Cicconi, D. Dobesh, B. Schroeder, T. Hayakawa, 93Nb NMR study of (K, Na)NbO_3-doped SiO_2–Na_2O–Al_2O_3 glasses, Phy. Status. Solidi. B 259 (2022) 2200016, https://doi.org/10.1002/pssb.202200016.

[83] W.R. Manning, O. Hunter, F.W. Calderwood, D.W. Stacy, Thermal expansion of Nb_2O_5, J. Am. Ceram. Soc. 55 (1972) 342–347, https://doi.org/10.1111/j.1151-2916.1972.tb11306.x.

[84] S.P. Ray, Preparation and characterization of aluminum borate, J. Am. Ceram. Soc. 75 (1992) 2605–2609, https://doi.org/10.1111/j.1151-2916.1992.tb05622.x.

[85] K. Kminikowska, D. Herman, A. Pander, Effect of $Al_4B_2O_9$ and $Al_{18}B_4O_{33}$ whiskers synthesized in situ on the evolution of microstructure and mechanical properties of white fused alumina and Cubitron glass-ceramic composites, J. Eur. Ceram. Soc. 43 (2023) 2564–2577, https://doi.org/10.1016/j.jeurceramsoc.2022.12.062.

[86] V.P. Klyuev, B.Z. Pevzner, Thermal expansion and transition temperature of glasses in the systems BeO–Al_2O_3–B_2O_3 and MgO–Al_2O_3–B_2O_3, J. Non-Cryst. Solids 353 (2007) 2008–2013, https://doi.org/10.1016/j.jnoncrysol.2007.01.065.

[87] Q. Fu, E.M. Aaldenberg, E.N. Coon, T.M. Gross, A.M. Whittier, B.M. Abel, D. E. Baker, Tough, bioinspired transparent glass-ceramics, Adv. Eng. Mater. 24 (2022) 2200350, https://doi.org/10.1002/adem.202200350.

[88] C.-H. Hsueh, P.F. Becher, Residual thermal stresses in ceramic composites. Part I: with ellipsoidal inclusions, Mater. Sci. Eng. A 212 (1996) 22–28, https://doi.org/10.1016/0921-5093(96)10176-3.

[89] O. Peitl, E.D. Zanotto, F.C. Serbena, L.L. Hench, Compositional and microstructural design of highly bioactive P_2O_5–Na_2O–CaO–SiO_2 glass-ceramics, Acta Biomater. 8 (2012) 321–332, https://doi.org/10.1016/j.actbio.2011.10.014.

[90] R.W. Davidge, T.J. Green, The strength of two-phase ceramic/glass materials, J. Mater. Sci. 3 (1968) 629–634, https://doi.org/10.1007/BF00757910.

[91] T. Du, X. Ge, F. Cao, H. Liu, C. Shi, J. Ding, D. Sun, Q. Zhang, Y. Yue, M. M. Smedskjaer, Structural origin of the deformation propensity of zeolitic imidazolate framework glasses, Chem. Mater. (2024). ⟨https://pubs.acs.org/doi/10.1021/acs.chemmater.4c00921⟩.

[92] D. Sun, T. Du, Q. Zhang, L.R. Jensen, D. Wang, J. Ding, J. Zhao, M.M. Smedskjaer, Toughening mechanism of barium titanosilicate glass-ceramics, Mater. Des. 246 (2024) 113303, https://doi.org/10.1016/j.matdes.2024.113303.

[93] X. Ren, T. Du, H. Peng, L.R. Jensen, C.A.N. Biscio, L. Fajstrup, M. Bauchy, M. M. Smedskjaer, Irradiation-induced toughening of calcium aluminoborosilicate glasses, Mater. Today Commun. 31 (2022) 103649, https://doi.org/10.1016/j.mtcomm.2022.103649.

[94] J. Wu, J.F. Stebbins, Temperature and modifier cation field strength effects on aluminoborosilicate glass network structure, J. Non-Cryst. Solids 362 (2013) 73–81, https://doi.org/10.1016/j.jnoncrysol.2012.11.005.

[95] X. Ren, P. Liu, S.J. Rzoska, B. Lucznik, M. Bockowski, M.M. Smedskjaer, Indentation response of calcium aluminoborosilicate glasses subjected to humid aging and hot compression, Materials 14 (2021) 3450, https://doi.org/10.3390/ma14133450.

[96] K. Januchta, R.E. Youngman, A. Goel, M. Bauchy, S.L. Logunov, S.J. Rzoska, M. Bockowski, L.R. Jensen, M.M. Smedskjaer, Discovery of ultra-crack-resistant oxide glasses with adaptive networks, Chem. Mater. 29 (2017) 5865–5876, https://doi.org/10.1021/acs.chemmater.7b00921.

[97] M.N. Svenson, T.K. Bechgaard, S.D. Fuglsang, R.H. Pedersen, A.Ø. Tjell, M. B. Østergaard, R.E. Youngman, J.C. Mauro, S.J. Rzoska, M. Bockowski, M. M. Smedskjaer, Composition-structure-property relations of compressed borosilicate glasses, Phys. Rev. Appl. 2 (2014) 024006, https://doi.org/10.1103/PhysRevApplied.2.024006.

[98] K.G. Aakermann, K. Januchta, J.A.L. Pedersen, M.N. Svenson, S.J. Rzoska, M. Bockowski, J.C. Mauro, M. Guerette, L. Huang, M.M. Smedskjaer, Indentation deformation mechanism of isostatically compressed mixed alkali aluminosilicate glasses, J. Non-Cryst. Solids 426 (2015) 175–183, https://doi.org/10.1016/j.jnoncrysol.2015.06.028.

[99] T.K. Bechgaard, A. Goel, R.E. Youngman, J.C. Mauro, S.J. Rzoska, M. Bockowski, L. R. Jensen, M.M. Smedskjaer, Structure and mechanical properties of compressed sodium aluminosilicate glasses: role of non-bridging oxygens, J. Non-Cryst. Solids 441 (2016) 49–57, https://doi.org/10.1016/j.jnoncrysol.2016.03.011.